Journal of Dynamics, Monitoring and Diagnostics, 2024, 3, 225-235
https://doi.org/10.37965/jdmd.2024.571

ISTP
RESEARCH ARTICLE

Identification of Stability Domains for Flow Parameters in Fused Filament Fabrication Using Acoustic Emission

Zhen Li,[1,2] Lei Fu,[2] Xinfeng Zou,[1,2] Baoshan Huang,[1] and Fengshou Gu[2]
[1]School of Industrial Automation, Beijing Institute of Technology, Zhuhai, Guangdong, China
[2]Centre for Efficiency and Performance Engineering, University of Huddersfield, Huddersfield, UK

(Received 12 June 2024; Revised 30 July 2024; Accepted 15 September 2024; Published online 18 September 2024)

Abstract: In Fused Filament Fabrication (FFF), the state of material flow significantly influences printing outcomes. However, online monitoring of these micro-physical processes within the extruder remains challenging. The flow state is affected by multiple parameters, with temperature and volumetric flow rate (VFR) being the most critical. The study explores the stable extrusion of flow with a highly sensitive acoustic emission (AE) sensor so that AE signals generated by the friction in the annular region can reflect the flow state more effectively. Nevertheless, the large volume and broad frequency range of the data present processing challenges. This study proposes a method that initially selects short impact signals and then uses the Fast Kurtogram (FK) to identify the frequency with the highest kurtosis for signal filtration. The results indicate that this approach significantly enhances processing speed and improves feature extraction capabilities. By correlating AE characteristics under various parameters with the quality of extruded raster beads, AE can monitor the real-time state of material flow. This study offers a concise and efficient method for monitoring the state of raster beads and demonstrates the potential of online monitoring of the flow states

Keywords: acoustic emission; center frequency; fast kurtogram; fused filament fabrication; stability domains

I. INTRODUCTION

Compared to traditional methods, Additive Manufacturing offers significant advantages in processing complex structures and provides greater freedom in geometric design [1,2]. The most commonly used method is material extrusion, known as Fused Deposition Modeling (FDM) or Fused Filament Fabrication (FFF), which reveals the manufacturing process through its name [3]. This technology constructs three-dimensional objects by heating and extruding plastic filament, depositing it layer by layer.

The raw material used in FFF is filamentous. The filament undergoes melting and squeezing, it is extruded at a set speed and state. This process is complex, and former investigations have attempted to model and validate process. The key to the continuous and stable extrusion of the molten material is to maintain a stable pressure drop inside the extruder. Bellini proposed a pressure drop model. The model assumes that the filament immediately melts upon entering the liquefied zone, and the solid filament acts like a piston pushing the liquid material. The model calculates the pressure drop at different positions, however, this model makes idealized assumptions about thermal melting and friction, and it overlooks the geometrical discrepancies between the filament and the inner diameter of the extruder nozzle. [4]. Osswald and colleagues improved the model, proposing that the filament primarily melts in the contraction region, forming a thin melt film [5]. The difference diameters between filament and extruder inner can generate a backflow region. The annular backflow is considered a failure mode in early research [6]. David D discovered that the backflow region forms a seal on the molten material, which is crucial for preventing the material from overflowing upwards [7]. This paper, based on the findings, analyzes the physical process of material extrusion and proposes a method for monitoring the stable flow of materials.

There are numerous methods for flow or extrusion monitoring, of which the imaging method is most applied for FFF monitoring [8]. Shahriar used an optical microscope to directly observe the raster beads, demonstrating the impact of temperature and VFR on extrusion quality [9]. Julian utilized X-ray computed tomography to perform imaging of the inner detail of flow, confirmed the presence of the annular backflow phenomenon [10]. Sietse modified the extruder, using weight sensors and pressure sensors to measure the total pressure and the pressure inside the nozzle for theoretical validation [11]. These methods to monitor flow conditions were primarily applied to validate theories and FE simulations, determining nozzle design and key operating parameters [12,13]. However, the methods are unsuitable for online monitoring of the printing process since they can possibly damage the structure of extruder. Therefore, more complex equipment and design are required.

The material flow inside the extruder generates weak stress waves, which can be captured by acoustic emission (AE) sensors [14]. The AE data collected from the nozzle are usually used for machine learning or neural networks to classify the flow state [15–17]. Compared to other monitoring methods, the AE method can use a single sensor to monitor the flow state online. Despite its convenience, data processing of the AE method lacks an explanation of the physical mechanisms.

This paper, based on recent studies of melt flow model, explains the mechanism of AE generation. However, the high sampling rate of AE technology generates large volumes of data. Additionally, due to the random microscale compression and deformation of materials, the

Corresponding author: Zhen Li (e-mail: zhen.li@hud.ac.uk).

characteristic signals show random, transient, high-frequency elastic waves. The collected signals contain transient elastic waves, background noise, and equipment influences, which must be considered when features are extracted.

The study proposes a data processing method for AE: First, short segments of waves containing impact signals are extracted in order to reduce data volume; then, Fast Kurtogram (FK) is utilized as the center frequency for band-pass filtering to calculate the frequency with the highest kurtosis. By comparing the results, the method greatly increases processing speed and improves the issue of weak features caused by the randomness in the elastic wave spectrum. Experiments were designed to collect AE signals under various parameters. By comparing these signals with extruded raster beads, the stable domain for flow parameters was validated. The main contributions are as follows:

i. The mechanism of AE generation from material flow within the extruder was analyzed.
ii. The processing speed of AE waveform signals and improved feature extraction was enhanced.
iii. The characteristics of AE over the parameter domain of temperature and VFR map the quality of the raster beads.

II. METHODS

A. FEED FORCE AND PRESSURE DROP MODEL

In the FFF process, the material is melted and extruded, the mechanism illustrated in the Fig. 1. The feed gear and idler wheel propel the filament, while the clamping force on the filament surface and the rotation of the driven gear are generating static friction that can push the filament into the liquefied region [18]. The pressure, P_{in}, acting on the extruder module by the driving force can be expressed as:

$$P_{in} = \frac{4F_{in}}{\pi {D_1}^2} \tag{1}$$

where F_{in} is the total driving force, D_1 is the diameter of filament.

As Fig. 2 shows, the pressure drop is divided into three parts in the liquefied zone: P_1 in the barrel region, P_2 in the contraction region, and P_3 in the capillary. The pressure drop across three parts can be calculated based on the parameters of the nozzle and the material [18]. The temperature and volumetric flow rate are the two critical parameters [19]. The pressure drop can be expressed as:

$$\Delta P_{total} = \Delta P_1 + \Delta P_2 + \Delta P_3 \tag{2}$$

Tomas Sculler proposed that the pressure drop includes contributions from the friction caused by the molten polymer in the backflow area [20]. Compared the pressure on the extruder head measured experimentally with the sum of the three pressure drops, the experimental values are higher, which proves the friction in the backflow region will generate an additional pressure drop [11]. P_f represents the pressure drop caused by the frictional force generated by shear force F_{shear}.

$$P_{in} = \Delta P_{total} + P_f \tag{3}$$

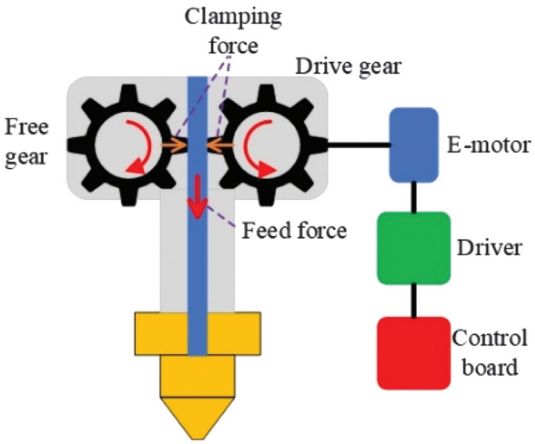

Fig. 1. Feed force generated by drive gear.

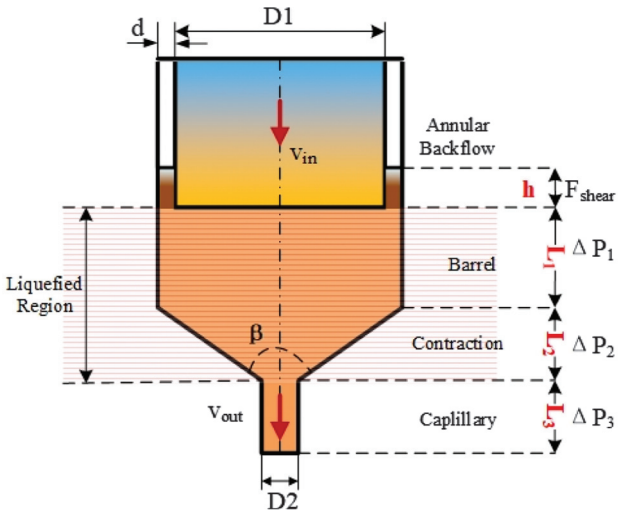

Fig. 2. Filament material liquefied in extruder.

B. SHEAR FORCE

The liquid material in the annular region provides shear stress to the nozzle wall. After melting, PLA material behaves as a non-Newtonian fluid, the shear stress τ can be calculated using the Power law model [21], as follows:

$$\tau = K\dot{\gamma}^n \tag{4}$$

where K is the flow consistency index that describes the viscosity characteristics of the fluid. $\dot{\gamma}$ represents the shear rate, which is the gradient change of the VFR. n is the flow behavior index, the material PLA exhibits shear-thinning behavior, where $0 < n < 1$.

For thermoplastic polymers, the flow consistency index K changes with temperature. The dependency can be expressed using the Arrhenius Equation, which relates the temperature to the viscosity behavior of the polymer:

$$K(T) = K_0 e^{-\frac{E_a}{R}\left(\frac{1}{T}-\frac{1}{T_0}\right)} \tag{5}$$

where T and T_0 represent the current temperature and reference temperature, respectively. $K(T)$ denotes the flow consistency index at temperature T. K_0 is the flow consistency index at the reference temperature T_0. E_a is the activation energy parameter that describes the sensitivity of K to changes in temperature. R is the universal gas constant.

In this study, the shear force in annular backflow region is considered, the shear rate in the gap can be simplify as $\frac{v}{d}$, where v is the filament feed speed, d is the gap distance between filament and nozzle inner wall. The shear rate can be express as:

$$\dot{\gamma} = \frac{4Q}{\pi {D_1}^2 d} \tag{6}$$

where Q is the VFR.

The Annual Backflow region affected by shear stress can be approximated as the contact area between the molten material and the inner walls. The shear force F_{shear} can be expressed as:

$$F_{shear} = \frac{4^n Q^n h}{\pi^{n-1} {D_1}^{2n-1} d^n} K_0 e^{-\frac{Ea}{R}\left(\frac{1}{T}-\frac{1}{T_0}\right)} \tag{7}$$

where h is the height of the backflow region, assumed to be constant because the filament material liquefies upon entering the liquefied zones and quickly forms a seal. From the equation, it is observed that only temperature T and volumetric flow rate Q serve as variables influencing the shear force. The shear force decreases with an increase in temperature and increases with an increase in volumetric flow rate.

C. AE RESPONSES IN FFF PROCESS

In the material flow process, shear forces between viscous materials and the wall of a nozzle act on microscopic asperities on the nozzle wall, resulting in viscous friction. As illustrated in Fig. 3, these microscopic asperities undergo forced deformation, quickly rebound, and release elastic waves, leading to AE behavior. Furthermore, another significant challenge is suitable features need to be extracted from the collected AE waveform signals to represent this physical process. Existing investigations on AE from viscous friction suggest that the root mean square (RMS) value of the AE signals produced by this process has a linear relationship with the power of friction [22–24], which can be represented as:

$$AE_{rms} = C\sqrt{\dot{U}_{shear}} \tag{8}$$

where $\dot{U}_{shear}$ represents the power of the shear stress in the active area, where C is a constant, which is the conversion ratio of the shear force to AE elastic wave energy and the preamplification ratio of the acquisition system.

$$\dot{U}_{shear} = F_{shear} v \tag{9}$$

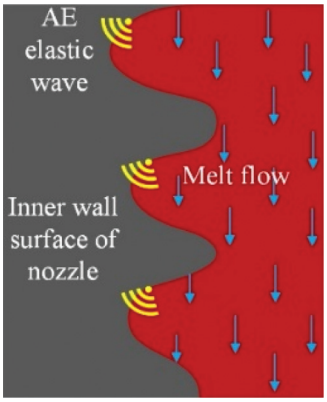

Fig. 3. Flow-Induced AE Elastic Waves from Micro Asperities.

where v is the velocity of the material flow inside the nozzle along the vertical direction. Substitute Equ. 7 into the equation, therefore, the RMS of the collected AE signal is:

$$AE_{rms} = C\sqrt{\frac{4^{n+1} Q^{n+1} h}{\pi^n {D_1}^{2n+1} d^n} K_0 e^{-\frac{Ea}{R}\left(\frac{1}{T}-\frac{1}{T_0}\right)}} \tag{10}$$

This equation describes the relationship between shear force and the root mean square (RMS) value of AE. Under constant material and environmental conditions, the RMS of AE is influenced by the material temperature and volumetric flow rate.

D. FAST KURTOGRAM

The FK is a tool used for analyzing and identifying transient characteristics and nonlinear features in signals. It is particularly effective for detecting anomalies and spikiness in signals, which often indicate the presence of transient impacts. This tool provides a powerful means for the precise detection of impact induced vibroacoustic signals [25–27].

Handling large volumes of high-sensitivity AE signals poses multiple challenges. The high sensitivity of these signals allows for the detection of minute physical changes but also captures a substantial amount of irrelevant noise and environmental disturbances. The high sampling rate characteristic generates a large amount of data, requiring significant computational power and time for storage and processing, which is not good to real-time monitoring applications. To solve these issues, short signals that contain clear impacts are extracted at first. Due to the wide-frequency characteristics of AE, the FK is used to calculate the Center Frequency (FC) and extract a self-adaptive feature band for filtering the impact signals. The approaches are depicted as follows.

Identify n impact points from the signal $S(t)$ through local querying:

$$\{P_{impact1}, P_{impact2}, \ldots, P_{impactn}\} = FindPeak(S(t), n) \tag{11}$$

Extract short segments of length L that contain all the energy of each impact point:

$$S_{local}(t)_i = S(t)t \in \left[\begin{array}{c} P_{impacti} - \frac{L}{2} \\ , P_{impacti} + \frac{L}{2} \end{array}\right] \tag{12}$$

The FK is also capable of describing the distribution of peaks in the frequency domain of a signal. The kurtosis for each frequency component can be described as:

$$Kur(f)_i = \frac{\sum_{t=1}^{N} \left(|FFT(S_{local}(t)_i)| - \mu\right)^4}{N\sigma^4} \tag{13}$$

where $Kur(f)$ is the kurtosis at frequency f where μ and σ are the mean and standard deviation of $|FFT(S_{local}(t)_i)|$ respectively, and N is the number of signal samples. The Center Frequency f_{center} can be found corresponding to the maximum kurtosis, as shown below:

$$f_{center} = argmax_f \; Kur(f) \tag{14}$$

The FK, serving as a crucial guiding parameter for the adaptive filtering band, is shown as follows:

$$FilterRange_i = [f_{centeri} - \Delta f, f_{centeri} + \Delta f] \tag{15}$$

where Δf is the chosen filtering band width.

E. OVERALL FRAMEWORK

This paper investigates the mechanism of AE generated within the extruder and utilizes extracted AE features to characterize the material flow state. To validate the proposed study, the research approach includes collecting AE waveforms generated inside the extruder and applying appropriate methods to extract features that reflect the flow characteristics under varying parameters.

To facilitate understanding of this paper, Fig. 4 presents an overview of the experimental and data analysis framework. The test bench includes a 3D printer, AE collection equipment, and modified parts.

The overall figure illustrates the analysis processing of an AE waveform to demonstrate the data processing approach. Figure 4(a) shows a raw AE waveform.

The previous analysis how material flow acts on microscopic asperities, leading to the instantaneous deformation rebound releasing AE elastic waves. Therefore, we consider that the impact signal can reflect the flow state. As Fig. 4(b) shows, Impacts are extracted from the AE waveform to obtain short signals, reducing computational demand, while still including the complete impact event.

Figure 4(c) displays the frequency spectrum of the impacts, which is found to have a random distribution. The AE waveform signals collected may from other sources and include noise, which the components are complex. To extract characteristics better, it is necessary to identify the frequency bands in which the elastic wave energy is concentrated.

Therefore, by utilizing the FK ability to process burst signals. As shown in Fig. 4(d), the locations of the highest kurtosis of frequency for different impact signals are marked with red circles. The frequency of the highest kurtosis represents the area where the impact energy is most concentrated. Band-pass filtering centered on the FC can removes noise, which unrelated to the flow state. As shown in Fig. 4(e), the filtered spectrum displays the primary frequency bands of the elastic wave.

The Fig. 4(f) explains how to construct a stable parameter domain. AE features under various parameters are used to construct a parameter domain. This domain, combined with equipment and material parameters, is compared with the corresponding quality of raster beads. It enables the prediction of the parameter range for stable material flow states through the parameter domain.

III. EXPERIMENTAL STUDY

To demonstrate the previous theoretical assumptions and verify the reliability and superiority of the proposed feature extraction algorithm, this chapter outlines an experiment designed to collect AE signals from a working printer extruder. The experiment was conducted under the hardware conditions available in our current laboratory. The experimental data include AE waveform signals under different working parameters.

A. EXPERIMENTAL PLATFORM

The objective of the experiment is to capture AE waveform signals generated by the minor flows inside the nozzle. As

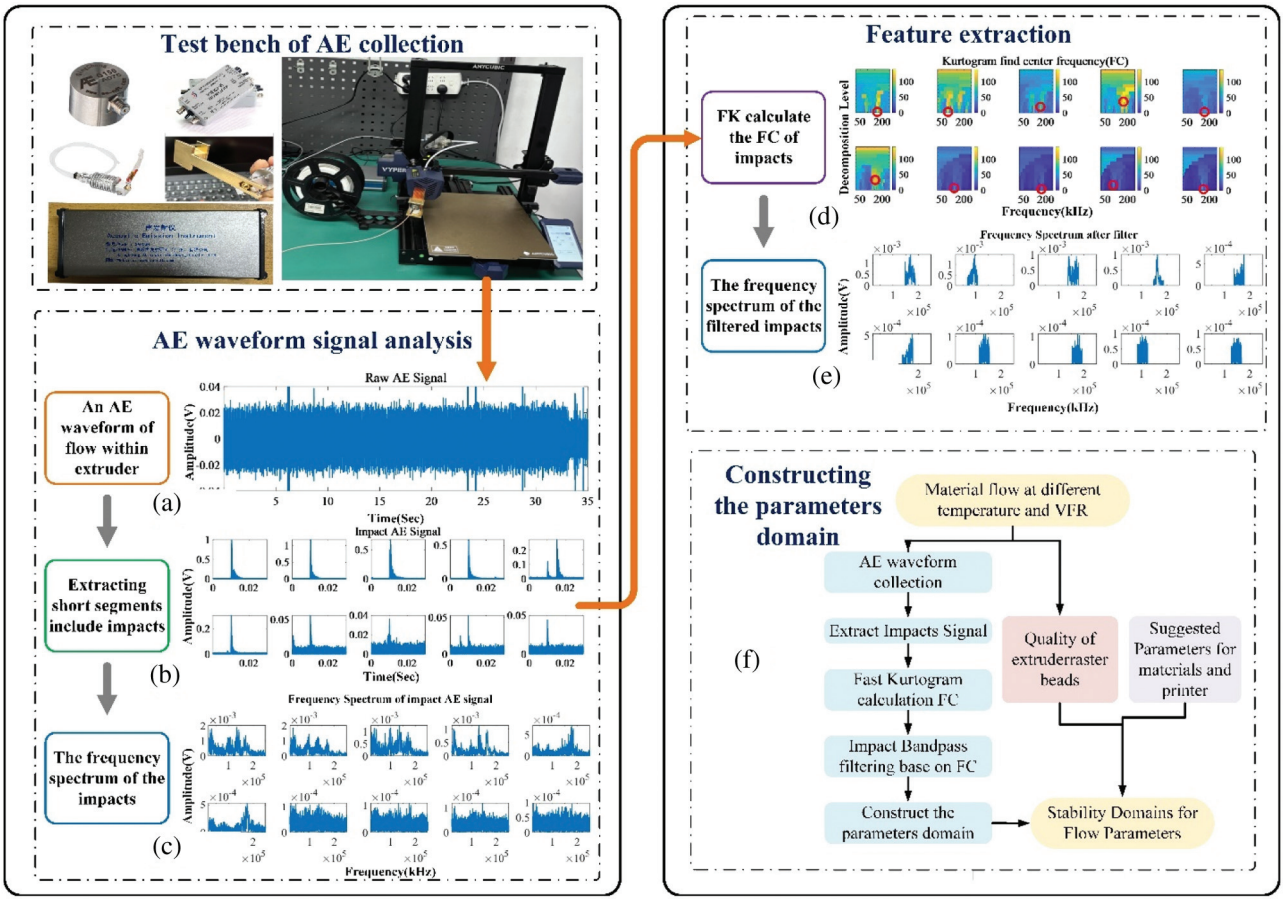

Fig. 4. Overall Framework of Study.

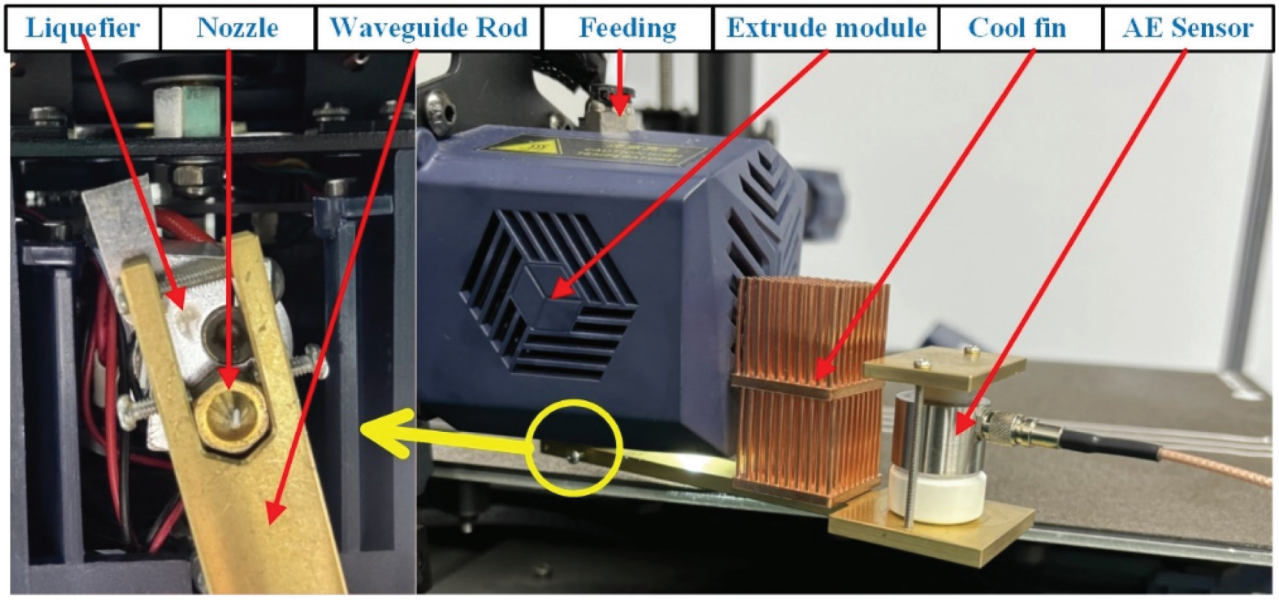

Fig. 5. Flow in FFF extruder on different parameters test bench.

Table I. Key printing parameters

Item	Key specifications
Nozzle Diameter	0.4 mm
Liquefier Diameter	2 mm
Filament Diameter	1.75 mm
Suggested Temperature	195–200°C
Scan Speed	20~100 mm/s
Suggested material type	PLA, TPU, ABS

shown in Fig. 5, a waveguide rod is designed to be installed on the nozzle, allowing the sensor to collect signals through this rod without interfering with the normal operation of the nozzle. Combining the printer's suggested dataset for the temperature and VFR, the chosen range of parameters exceeded the normal operating conditions, but the extruder can inject out the material raster.

The parameters are set as follow:

i. The nozzle temperature is initially set at 180°C and then increased incrementally by 2°C up to 200°C, resulting in a total of 11 temperature settings. The suggested range is 195–200°C.

ii. The VFR of material flow set 6 degrees, from 3.2 mm^3/s and increased incrementally by 3.2 up to 19.2 mm^3/s. the suggest range is 6.4–12.8 mm^3/s.

In this study, a FFF 3D printer was utilized for experiments. This printer with an open gantry structure and open-source control facilitates the installation of sensors and control of experimental parameters. The primary parameters in this study are shown in Table I.

B. MARTERIAL PROPERTIES

Polylactic Acid (PLA) was selected as the material for this experiment. PLA is a widely used biodegradable thermoplastic polymer in 3D printing, known for its stable rheological properties within the common printing temperature range. This stability is beneficial for ensuring consistency in the experimental material and continuity in the process.

Table II. PLA parameters

Type	Diameter	Melting point	Heat distortion temperature
PLA	1.75 mm	162.4°C	52–58°C

In FFF, the temperature of the nozzle plays a critical role in influencing the flow of the molten material. The viscosity of the molten material is significantly affected by temperature; for PLA (polylactic acid) material, viscosity decreases as the temperature increases [28].

The main parameters relevant to the material are presented in Table II.

C. COLLECT OF AE SIGNALS

The AE signals generated by the material flow inside the nozzle are relatively weak, making the selection of appropriate sensors and the setting of proper parameters crucial for signal collection. In this study, the design of the waveguide rod enabled direct data collection near the nozzle's proximal end. The AE sensor was affixed to the surface of the waveguide rod with a coupling agent to ensure maximum sensitivity and the shortest signal transmission path. The sensor's sampling rate was set at 1 MHz, ensuring the capture of minute AE elastic waves. A four-channel high-speed acquisition card from Qingcheng Company was used, guaranteeing high data throughput. Table III below presents the main sensor parameters and acquisition system settings used for signal collection.

Table III. AE Signal acquisition settings

Operating temperature	Frequency band	Peak sensitivity	Pre-gain
–20–120°C	20–400 kHz	75 dB	60 dB

IV. RESULT AND DISCUSSION

Through experiments, AE signals from the nozzle were collected at 11 different temperature states and 6 VFR degrees. Signals at three significantly different temperatures—180°C, 190°C, and 200°C—were selected to analyze time-frequency characteristics and power spectra, with little difference observed in the time-domain signals. Three VFR degrees were chosen for comparison. Due to the high sampling rate, the volume of data was huge, leading to excessive computational load and prolonged computer processing times. To address this issue, a new data analysis method was proposed. It starts by extracting short segments of data where impacts occur, then rapidly identifies the center of frequency (FC) of each impact using FK and finally filters the signals using the identified center frequencies. The characteristics of the original and the impact signals were compared at the end.

A. RAW SIGNAL CHARACTERISTICS AT DIFFERENT PARMETERS

First, the raw signals are compared. The experiment compares the time-frequency characteristics of AE when there are variations in two groups of variables: material temperature and VFR. This analysis includes a comparison of the time domain, frequency domain, and power spectrum. Figure 6 shows the time domain signals for two groups. Figure 6(a)–(c) illustrate the AE waveforms at three typical temperatures, from high to low. Figure 6(d)–(f) display the waveforms for three different VFR. When the parameters change slowly, it is difficult to directly observe differences from the time-domain signals.

Figure 7 compares the frequency spectra and power spectra of two sets of parameters, which the frequency band was between 20 and 250 kHz. While the frequency bands vary widely, and their locations are random and discontinuous. It can be observed that the power spectra of the two parameter sets show trends of variation under different parameters, but the changes are not significant. This indicates that the proportion of noise in the signals is too high, need further feature extraction.

If Fig. 7(b) and (d) are compared, it can be found that the influence of VFR changes on the power spectrum is more pronounced than that of temperature changes. The influence of two sets on AE characteristics will be further compared in subsequent analyses.

B. IMPACT SIGNAL CHARACTERISTICS AT DIFFERENT PARMETERS

In the section illustrating methods, the physical mechanisms of AE impacts were analyzed, demonstrating that impact signals effectively characterize flow states. Additionally, cutting short signal segments containing impacts reduces the data volume caused by high sampling rates.

Figure 8(a)–(c) display the impact signals with the highest amplitude as the temperature decreases, showing peak values at 200°C, 190°C, and 180°C of 0.03V, 0.05V, and 0.3V, respectively. Figure 8(d)–(f) illustrate the

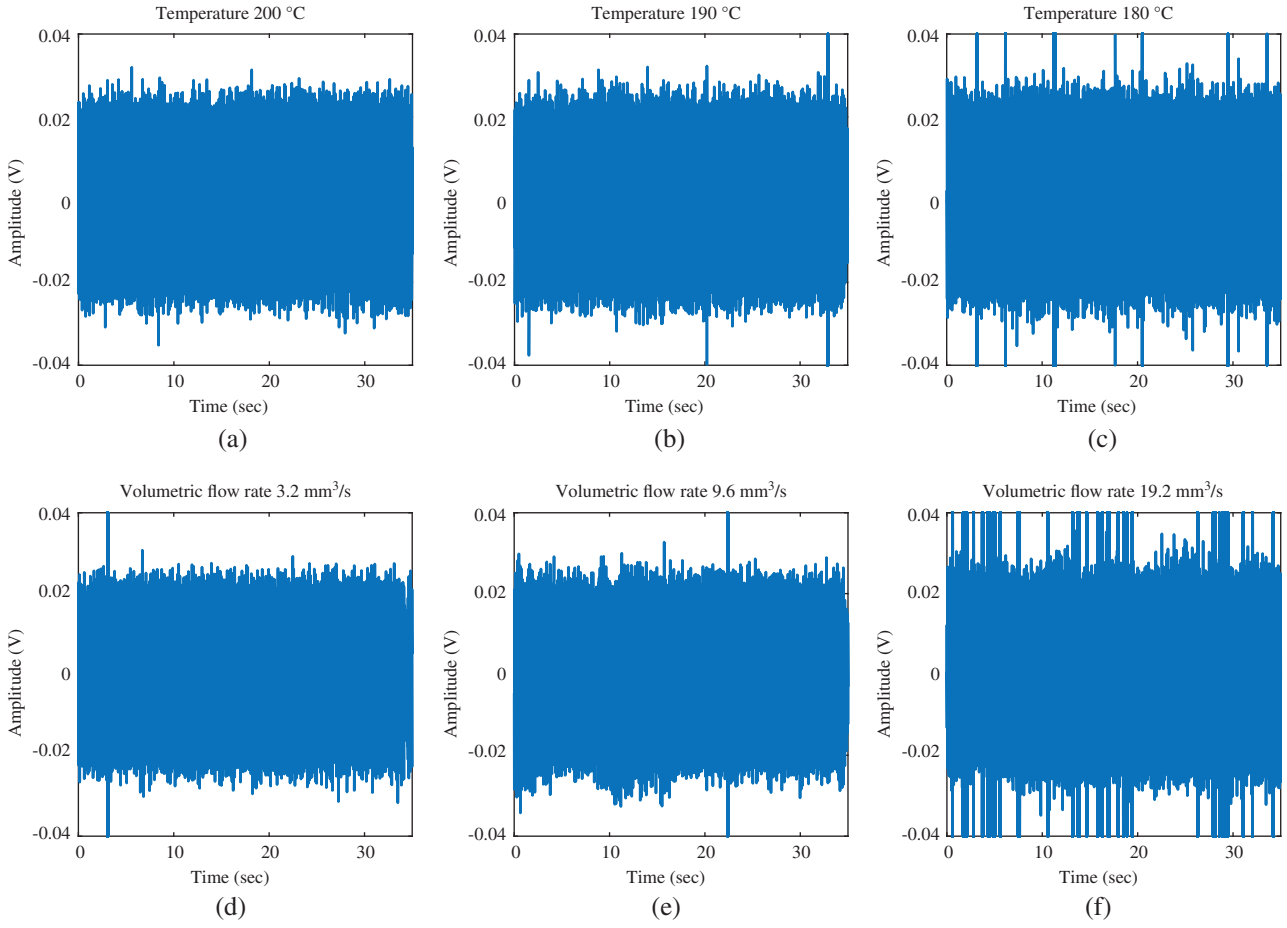

Fig. 6. Raw signals analysis of time domain in different parameters.

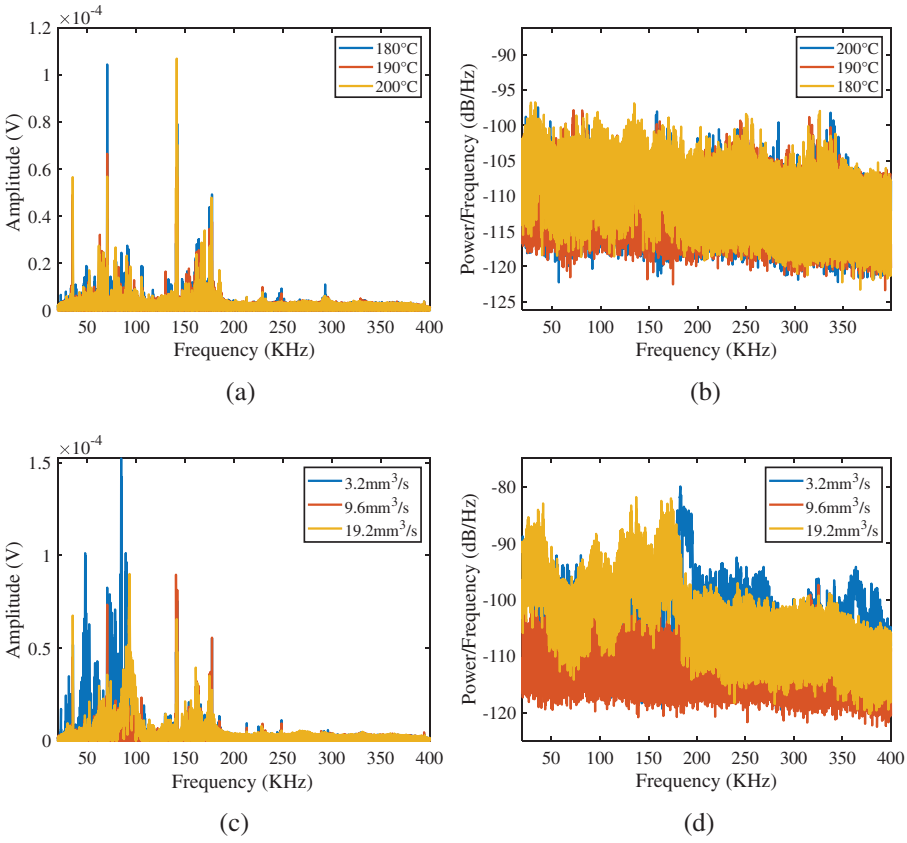

Fig. 7. Raw signals analysis of Frequency domain and Power Spectral Density.

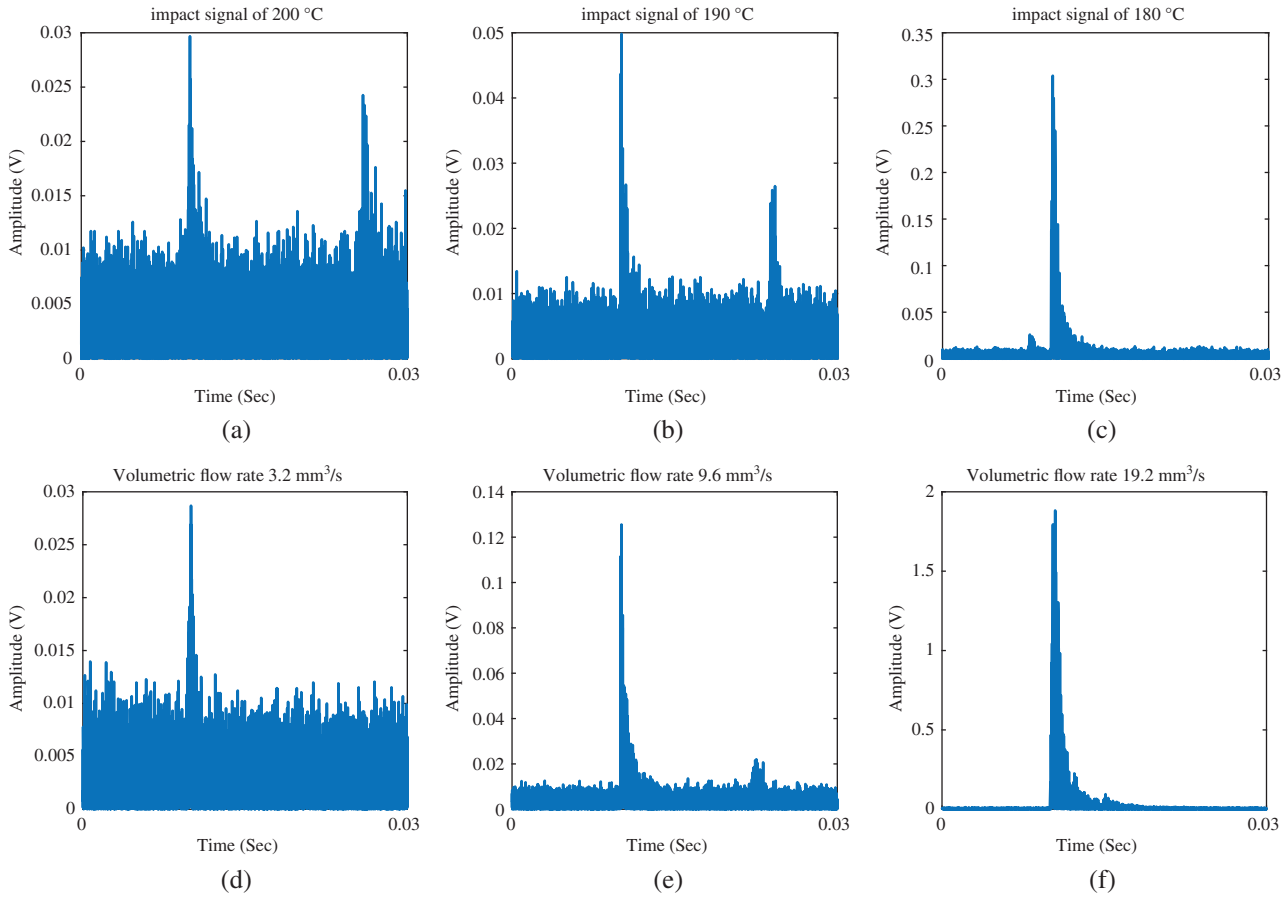

Fig. 8. Time domain analysis of impact signals in different parameters.

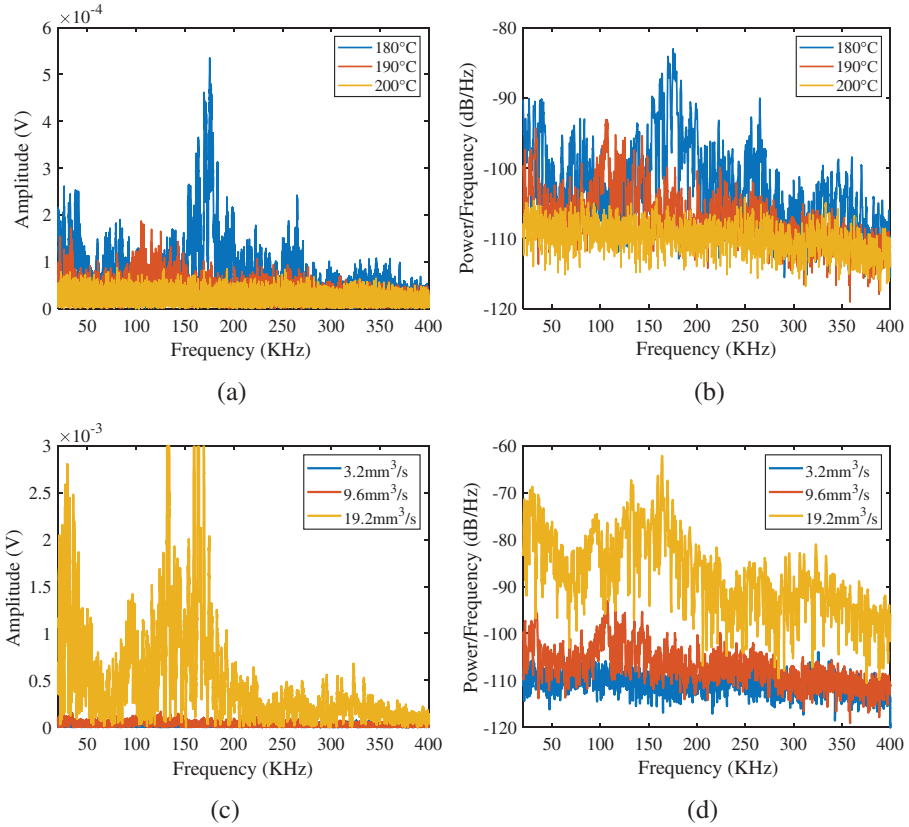

Fig. 9. Impact signals analysis of Frequency domain and Power Spectral Density.

maximum impacts with increasing volumetric flow rates (VFR), with peak values at 3.2 mm^3/s, 9.6 mm^3/s, and 19.2 mm^3/s of 0.028V, 0.125V, and 1.9V, separately. Comparing the peak values of AE impacts for the two parameters, VFR has a greater effect on the flow state than temperature within the selected range.

Figure 9(a) and (c) show the frequency spectrum of impact signals, with observable differences in amplitudes. The power spectrums in Fig. 9(b) and (d) indicate that, compared to raw signals, impact signals exhibit more distinct differentiation in the power spectrum. However, these features display significant randomness, likely related to the broadband characteristics of AE signals.

The analysis highlights that although impact signals perform well in the power spectrum, the complex components of AE signals necessitate identifying frequency bands where impact energy is concentrated to reduce noise interference, thereby enhancing the AE characteristics generated by the flow.

C. EXTACTION OF CENTRAL FREQUENCY BY FK ANALYSIS

The former section has demonstrated the capability of impact signals to characterize flow states. However, the analysis of their power spectra occurs over a wide frequency range, and the power spectra of different impacts exhibit randomness.

The FK is particularly suitable for analyzing non-stationary signals that include bursts of high-frequency components. This method, with examination of multiple frequency resolutions and levels of kurtosis, can determine which frequency band contains the key information about impact events, making it ideal for selecting the optimal frequency band.

Considering the impact characteristics of the signals, FK is introduced to decompose segments of impact signals. Choose the decomposition degree as 6 level. As shown in Fig. 10, there are frequency-kurtosis heatmap for six impact events from the same waveform signal. The red circles mark the frequency positions with the highest kurtosis of the impact signals. The positions of the highest kurtosis vary, which also indicates that the central frequency of each impact signal is uncertain. Through this method, the central frequency of the impact can be determined, with the energy of the impact concentrated near the central frequency.

Therefore, using the central frequency (FC) for band-pass filtering can reduce other signals in the AE signals that are unrelated to the flow. This part of the noise may originate from other noise sources or the background noise of the collection system. Here, the function of FK is to determine the central frequency of the frequency band for band-pass filtering. This method can adapt to different impacts, overcome the randomness of impact signals, and enhance the characteristics related to transient elastic waves caused by flow."

D. FEATURE EXTRATION AND RASTER QUALITY

According to the theoretical analysis in Section II, the lower the temperature in the nozzle, the higher the viscosity consistency coefficient of the material flow, consequently it results in higher AE power and higher RMS values of the

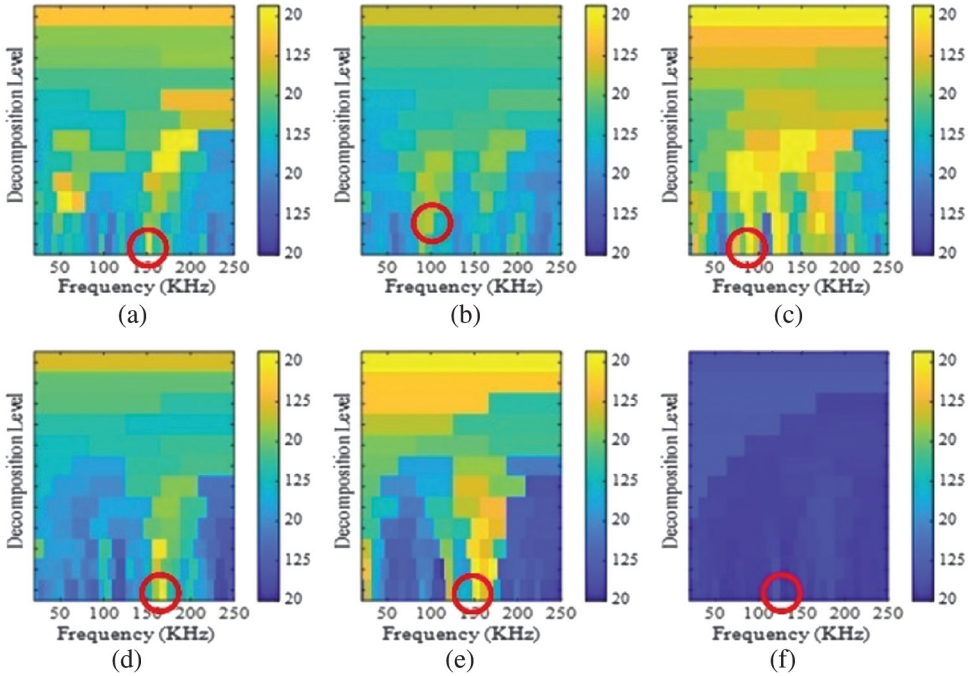

Fig. 10. Fast Kurtogram Frequency-Kurtosis Distribution Heatmaps.

signal. And higher VFR results in higher AE power. This study introduces a data processing method that uses FK to extract features from small datasets of impact signals. Figures 11 and 12 presents the RMS values obtained through four different methods: the raw signal, the impact signal, the raw signal with FK band-pass filtering, and the impact signal with self-adaptive FK band-pass filtering. The two sets of parameters: temperature and VFR are compared.

In the temperature group, as shown in Fig 11, RMS values from the raw signals and after filtering shows poor distinction between the parameter ranges, i.e. it is hard to identify the change in temperature from 184°C to 186°C. The two methods use impact signals demonstrate better performance than the first two. However, the red line, representing the impact signal without self-adaptive band-pass filtering, shows an outlier at 182°C. In contrast, the green line, which represents the impact signal with self-adaptive band-pass filtering, which corrected the anomaly at 182°C, showing an improved trend.

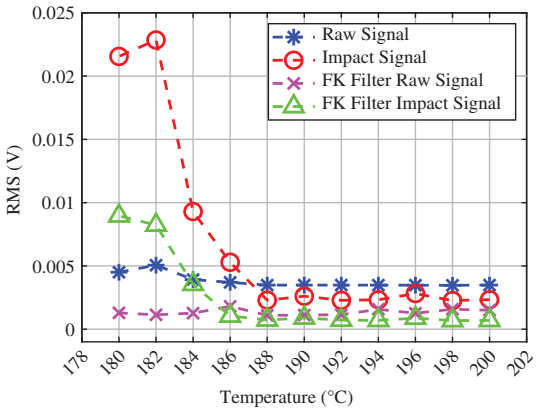

Fig. 11. RMS Values of temperature.

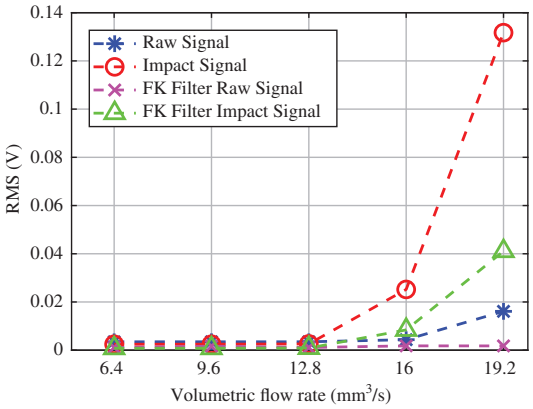

Fig. 12. RMS Values of VFR.

The VFR group is showing similar trend in Fig. 12 in which two impact signals gave better characteristics. but in the low VFR degree, it has no discrimination.

Overall, impact signals provide better characterization. Self-adaptive filtering methods can correct some anomalies, resulting in more accurate trend representation. The analysis results show correlations with the theoretical analysis presented in Section II.

By comparing the same set of experimental data through four different methods, the theory that temperature and VFR affect material flow in the nozzle has been validated. The new data processing method proposed shows improved performance in feature extraction. However, the two graphs in Figs. 11 and 12 are compared, which reveals that the ranges of changes for the two types of parameters are on different orders of magnitude. The impact of VFR on AE characteristics is significantly greater than that of temperature. Both parameters influence the friction in the annular backflow region within the nozzle. There is a

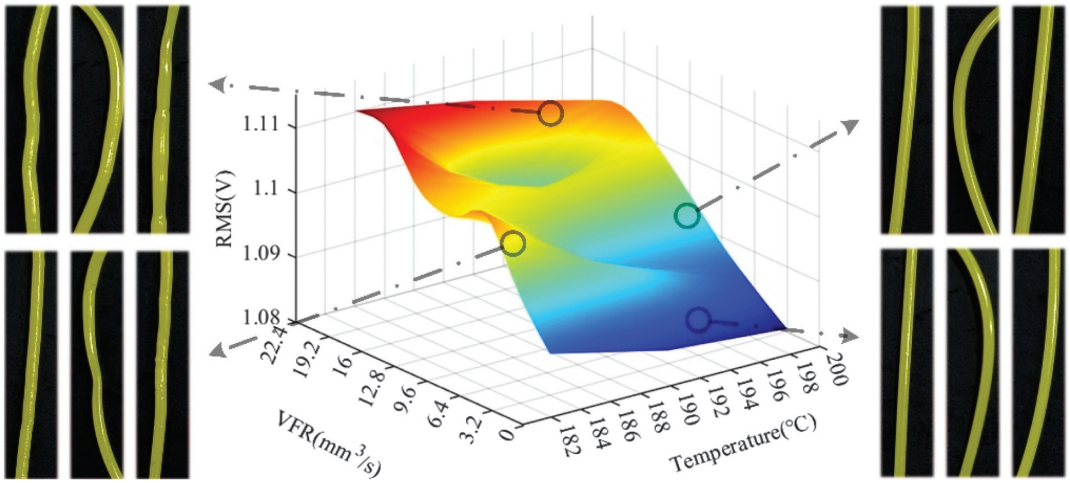

Fig. 13. The parameters stability domain for AE features and the printed raster quality distributes at the domain.

stability domain that ensures the flow state and the quality of the raster.

The Fig. 13 shown the characteristic domain of AE formed by the two parameters. Parameters combinations are analyzed from the four edges of the defined region for real raster printing. The four selected parameter combinations represent high and low VFR at normal temperature, and high and low temperature at normal VFR. The two warm-colored points corresponding to low temperature and high VFR exhibit significant quality defects in the printed raster. These defects include a rough surface and unstable diameter, indicating oscillations in the flow state. The two cool-colored points correspond to good surface quality, with the raster being uniform and stable.

V. CONCLUSIONS

i. Based on the existing nozzle material flow model, it is inferred that the additional pressure drop caused by material friction in the annular backflow region can be captured by AE sensors located on the proximal end of the nozzle. Theoretical analysis has demonstrated the correlation between the additional pressure drop with the two parameters, material temperature and volumetric flow rate. Data analysis has shown that the RMS value of AE waveform signals effectively represents frictional power, thereby allowing for the assessment of the flow state.

ii. After large volumes of high-sampling-rate AE data were collected, a method based on the Fast Kurtogram (FK) was proposed to extract features from short, transient signals. The FK self-adaptive center frequency filtering method effectively addresses the issue of the random distribution of impact signal center frequencies across a wide bandwidth by automatically selecting the most suitable band-pass filter. Compared to directly analyzing raw signals, the proposed method significantly improves data processing speed and enhances feature extraction capabilities.

iii. The AE characteristics correspond to a parameter domain composed of material temperature and volumetric flow rate (VFR), which can be mapped to the quality of the extruded raster. By comparing signal characteristics with printing quality, it has been found that the constructed parameter domain can predict raster quality, providing a valuable reference for selecting parameter combinations.

CONFLICT OF INTEREST STATEMENT

The authors declare no conflicts of interest.

REFERENCES

[1] A. Das, E. L. Gilmer, S. Biria, and M. J. Bortner, "Importance of polymer rheology on material extrusion additive manufacturing: correlating process physics to print properties," *ACS Appl. Polym. Mater.*, vol. 3, pp. 1218–1249, 2021.

[2] M. Harris, J. Potgieter, R. Archer, and K. M. Arif, "Effect of material and process specific factors on the strength of printed parts in fused filament fabrication: a review of recent developments," *Mater. (Basel).*, vol. 12, no. 10, p. 1664, 2019.

[3] M. Koç, "Fused filament fabrication process: a review of numerical simulation techniques," *Polymers (Basel).*, vol. 13, p. 3534, 2021.

[4] A. Bellini and M. Bertoldi, "Liquefier dynamics in fused," *J. Manuf. Sci. Eng.*, vol. 126, pp. 237–246, 2004.

[5] T. A. Osswald, J. Puentes, and J. Kattinger, "Fused fi lament fabrication melting model," *Addit. Manuf.*, vol. 22, pp. 51–59, 2018.

[6] J.-P. K. H. Valkenaers, F. Vogeler, E. Ferraris, and A. Voet, "A novel approach to additive manufacturing: screw extrusion 3D-printing," *10th Int. Conf. Multi-Mater. Micro Manuf.*, pp. 3–6, 2013. DOI: 10.3850/978-981-07-7247-5-359.

[7] D. D. Phan, J. S. Horner, Z. R. Swain, A. N. Beris, and M. E. Mackay, "Computational fluid dynamics simulation of the melting process in the fused filament fabrication additive manufacturing technique," *Addit. Manuf.*, vol. 33, p. 101161, 2020.

[8] C. Liu, A. Chung, C. Law, D. Roberson, and Z. J. Kong, "Image analysis-based closed loop quality control for additive manufacturing with fused fi lament fabrication," *J. Manuf. Syst.*, vol. 51, pp. 75–86, 2019.

[9] S. Bakrani, F. Chabert, V. Nassiet, and A. Cantarel, "Influence of printing parameters on the stability of deposited beads in fused filament fabrication of poly (lactic) acid," *Addit. Manuf.*, vol. 25, pp. 112–121, 2019.

[10] J. Kattinger, M. Kornely, J. Ehrler, C. Bonten, and M. Kreutzbruck, "Analysis of melting and flow in the hot-end of a material extrusion 3D printer using X-ray computed tomography," *Addit. Manuf.*, vol. 76, p. 103762, 2023.

[11] S. De Vries, T. Schuller, F. J. Galindo-rosales, and P. Fanzio, "Pressure drop non-linearities in material extrusion additive manufacturing: a novel approach for pressure monitoring and numerical modeling," *Addit. Manuf.*, vol. 80, p. 103966, 2024.

[12] E. L. Gilmer et al., "Model analysis of feedstock behavior in fused fi lament fabrication: Enabling rapid materials screening," *Polym. (Guildf).*, vol. 152, pp. 51–61, 2018.

[13] X. Xu, H. Ren, S. Chen, X. Luo, F. Zhao, and Y. Xiong, "Review on melt flow simulations for thermoplastics and their fiber reinforced composites in fused deposition modeling," *J. Manuf. Process.*, vol. 92, pp. 272–286, 2023.

[14] P. Ranjan, P. Ambily, P. Sanker, S. Sebastian, and S. Kumar, "A review on application of acoustic emission testing during additive manufacturing," *J. Nondestruct. Eval.*, vol. 42, no. 4, pp. 1–31, 2023.

[15] H. Li, Z. Yu, F. Li, Q. Kong, and J. Tang, "Real-time polymer flow state monitoring during fused filament fabrication based on acoustic emission," *J. Manuf. Syst.*, vol. 62, pp. 628–635, 2022.

[16] Y. Lu and Y. Wang, "Active physics-constrained dictionary learning to diagnose nozzle conditions in fused filament fabrication process," *Manuf. Lett.*, vol. 35, pp. 973–982, 2023.

[17] K. Xu, J. Lyu, and S. Manoochehri, "In situ process monitoring using acoustic emission and laser scanning techniques based on machine learning models," *J. Manuf. Process.*, vol. 84, pp. 357–374, 2022.

[18] M. Moretti, A. Rossi, and N. Senin, "In-process simulation of the extrusion to support optimisation and real-time monitoring in fused filament fabrication," *Addit. Manuf.*, vol. 38, p. 101817, 2021.

[19] R. Badarinath and V. Prabhu, "Real-time sensing of output polymer flow temperature and volumetric flowrate in fused filament fabrication process," *Mater. (Basel)*, vol. 15, p. 618, 2022.

[20] T. Schuller, P. Fanzio, and F. J. Galindo-rosales, "Analysis of the importance of shear-induced elastic stresses in material," *Addit. Manuf.*, vol. 57, p. 102952, 2022.

[21] M. Kaseem and Y. Gun, "Melt flow behavior and processability of polylactic acid/polystyrene (PLA/PS) polymer blends," *J. Polym. Environ.*, vol. 25, no. 4, pp. 994–998, 2017.

[22] H. A. Kishawy, "Application of acoustic emissions in machining processes: analysis and critical review," *Int. J. Adv. Manuf. Technol.*, vol. 98, pp. 1391–1407, 2018.

[23] S. Liu, X. Wang, Z. Liu, Y. Wang, and H. Chen, "Machined surface defects monitoring through VMD of acoustic emission signals," *J. Manuf. Process.*, vol. 79, pp. 587–599, 2022.

[24] H. Towsyfyan, F. Gu, A. D. Ball, and B. Liang, "Tribology international modelling acoustic emissions generated by tribological behaviour of mechanical seals for condition monitoring and fault detection," *Tribiol. Int.*, vol. 125, pp. 46–58, 2018.

[25] L. Wang, Z. Liu, Q. Miao, and X. Zhang, "Time – frequency analysis based on ensemble local mean decomposition and fast kurtogram for rotating machinery fault diagnosis," *Mech. Syst. Signal Process.*, vol. 103, pp. 60–75, 2018.

[26] Ã. Antoni, "Fast computation of the kurtogram for the detection of transient faults," *Mech. Syst. Signal Process.*, vol. 21, pp. 108–124, 2007.

[27] Y. Lei, J. Lin, Z. He, and Y. Zi, "Application of an improved kurtogram method for fault diagnosis of rolling element bearings," *Mech. Syst. Signal Process.*, vol. 25, no. 5, pp. 1738–1749, 2011.

[28] M. Shahnooshi, A. Javadi, H. Nazockdast, and K. Ottermann, "Rheological rationalization of in situ nanofibrillar structure development: tailoring of nanohybrid shish-kebab superstructures of poly (lactic acid) crystalline phase," *Polymer*, vol. 211, p. 123040, 2021.